

Gigantic Magnetochiral Anisotropy in the Topological Semimetal ZrTe_5

Yongjian Wang¹, Henry F. Legg^{2,3}, Thomas Bömerich², Jinhong Park², Sebastian Biesenkamp¹,

A. A. Taskin¹, Markus Braden¹, Achim Rosch², and Yoichi Ando^{1,*}

¹*Physics Institute II, University of Cologne, Zùlpicher Straße 77, 50937 Köln, Germany*

²*Institute for Theoretical Physics, University of Cologne, Zùlpicher Straße 77, 50937 Köln, Germany*

³*Department of Physics, University of Basel, Klingelbergstrasse 82, CH-4056 Basel, Switzerland*

 (Received 23 December 2021; revised 22 February 2022; accepted 31 March 2022; published 29 April 2022)

Topological materials with broken inversion symmetry can give rise to nonreciprocal responses, such as the current rectification controlled by magnetic fields via magnetochiral anisotropy. Bulk nonreciprocal responses usually stem from relativistic corrections and are always very small. Here we report our discovery that ZrTe_5 crystals in proximity to a topological quantum phase transition present gigantic magnetochiral anisotropy, which is the largest ever observed to date. We argue that a very low carrier density, inhomogeneities, and a torus-shaped Fermi surface induced by breaking of inversion symmetry in a Dirac material are central to explain this extraordinary property.

DOI: [10.1103/PhysRevLett.128.176602](https://doi.org/10.1103/PhysRevLett.128.176602)

The magnetochiral anisotropy (MCA) is a nonreciprocal transport effect induced by an external magnetic field in a chiral or polar system without inversion symmetry. Nonreciprocal response means that the resistance R of a material is different for electrical current \mathbf{I} flowing to the right ($+I$) and to the left ($-I$), which immediately implies broken inversion symmetry. Remarkably, nonreciprocal transport can be triggered and controlled by external magnetic fields. Depending on the mechanism, there are two possible types of the nonreciprocal resistance [1]: one is the inner-product type [2] expressed by $R = R_0[1 + \gamma(\mathbf{B} \cdot \mathbf{I})]$ (where R_0 is the reciprocal resistance and γ is a numerical coefficient), and the other is the vector-product type [3] expressed by $R = R_0[1 + \gamma(\hat{\mathbf{P}} \times \mathbf{B}) \cdot \mathbf{I}]$, where $\hat{\mathbf{P}}$ is a unit vector which characterizes the axis of the nonreciprocal effect. The spin texture of Fermi surfaces in topological materials can give rise to such MCAs, with known examples of both types [1].

The coefficient $\gamma \equiv [(R/R_0) - 1]/(|\mathbf{B}| \cdot |\mathbf{I}|)$, obtained for $\mathbf{B} \parallel \mathbf{I}$ for the inner-product type and for $\mathbf{B} \perp \mathbf{I}$ with $(\mathbf{B} \times \mathbf{I}) \perp \hat{\mathbf{P}}$ for the vector-product type, is usually used as a measure of the MCA [1]. However, this γ depends on the shape and size of the specimen used for the measurement, and a better measure for a bulk material is the normalized coefficient $\gamma' \equiv A_{\perp} \gamma$, where A_{\perp} is the cross section of the specimen [4]. As a materials property, the MCA is usually of relativistic origin and has been ubiquitously found to be very small. Recently, tellurium was shown to have an inner-product type MCA with $|\gamma'|$ of $10^{-8} \text{ m}^2 \text{ T}^{-1} \text{ A}^{-1}$ [5], which is the largest reported as a bulk property. It was theoretically predicted that the chiral anomaly in Weyl semimetals may lead to a large MCA of the inner-product type [6], but there has been no confirmation. In this Letter,

we report that topological semimetal ZrTe_5 presents a vector-product type MCA with $|\gamma'|$ of up to $4 \times 10^{-7} \text{ m}^2 \text{ T}^{-1} \text{ A}^{-1}$ as its bulk property.

ZrTe_5 has an orthorhombic layered structure which nominally belongs to the $Cmcm (D_{2h}^{17})$ space group [7] (the actual symmetry is, however, lower, see below). The crystal structure consists of two-dimensional (2D) layers stacked along the b axis via van der Waals interactions [Fig. 1(a)]. In each layer (i.e., ac plane), ZrTe_5 chains running along the a axis provide the highest conductivity along the a axis. In transport studies, the principal crystal axes a , c and b correspond to the directions x , y and z , respectively [7]. Bulk single crystals of ZrTe_5 have been a focus of significant interest in recent years [8–16], with major discoveries such as chiral magnetic effect [10], unconventional anomalous Hall effect [12], and three-dimensional (3D) quantum Hall effect [15]. While initially there was a debate about the electronic structure realized in ZrTe_5 , it is now generally believed that in most samples there is a temperature-driven transition from a strong 3D topological insulator (TI) phase to a weak 3D TI phase with increasing temperature and that a pronounced resistivity peak marks a gapless semimetal realised between the two gapped TI phases [8], although there are still other interpretations [17,18]. In this work, we focus on ZrTe_5 crystals (grown by a Te-flux method [19]) whose resistivity is maximum at base temperature [Fig. 1(b)], suggesting that the system has been tuned to a semimetallic state. Our detailed data discussed below indeed support the realization of the semimetallic state.

As was already reported [13,14], these semimetal samples in perpendicular magnetic fields present unconventional magnetoresistance, which is singular at low fields and saturates in high fields, as shown in the inset of Fig. 1(b)

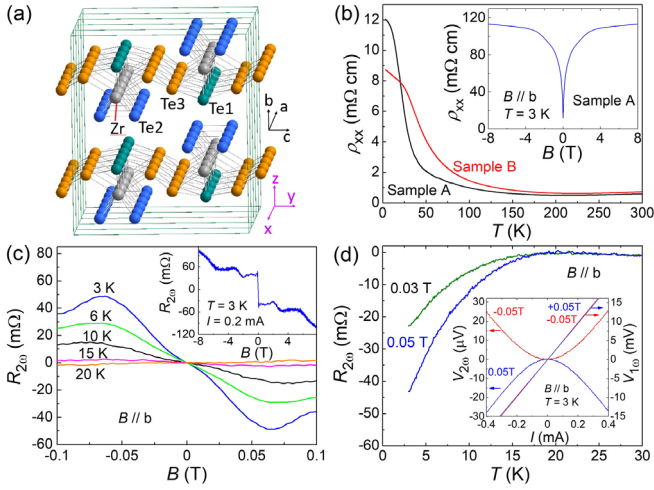


FIG. 1. Structure and transport properties of ZrTe₅. (a) Layered crystal structure of ZrTe₅ (b) Temperature dependence of the resistivity ρ_{xx} of samples A and B measured with $I \parallel a$. Inset: magnetoresistance of sample A for $B \parallel b$ at 3 K. (c) Magnetic-field dependence of the second-harmonic component of the resistance, $R_{2\omega}$, of sample A in $B \parallel b$ for low fields at various temperatures; inset shows the data at 3 K for a wider range of B up to ± 8 T. (d) Temperature dependence of $R_{2\omega}$ of sample A measured in $B \parallel b$. Inset: Current dependencies of the first- and second-harmonic voltages, $V_{1\omega}$ and $V_{2\omega}$, in $+0.05$ and -0.05 T at 3 K; the slight difference in $V_{1\omega}$ for opposite B is due to a small admixture of Hall voltage. Throughout this paper, whenever $R_{2\omega}$ is shown, it was measured with $I_{ac} = I_0/\sqrt{2} = 0.2$ mA.

for sample A. We measured the resistivity ρ_{xx} with a low-frequency AC excitation $I = I_0 \sin \omega t$ along the a axis and, when the second-harmonic component $R_{2\omega}$ was probed, we discovered an unusually large signal [Fig. 1(c) inset] whose magnetic-field (B) dependence is totally different from that of the first harmonic. As discussed in Ref. [19], this $R_{2\omega}$ directly reflects γ . Note that the physics behind $R_{2\omega}$ is totally different from the second-harmonic generation in the optical range [32–35], which is a photonic process at much higher energy [1]. The main panel of Fig. 1(c) shows that $|R_{2\omega}|$ grows rapidly and almost linearly with B in a narrow range

of $|B| \lesssim 0.06$ T. This component shows up only below 20 K [Fig. 1(d)]. The second-harmonic voltage $V_{2\omega}$ depends quadratically on the current I , is observed for $\mathbf{B} \perp \mathbf{I}$, and is antisymmetric with respect to B [Fig. 1(d), inset], which is the behavior expected for the vector-product type, $V_{2\omega} = \gamma R_0 I (\hat{\mathbf{P}} \times \mathbf{B}) \cdot \mathbf{I}$. In contrast, the first-harmonic voltage $V_{1\omega}$ is linear in I and symmetric with respect to B [Fig. 1(d) inset].

To identify the axis of the characteristic unit vector $\hat{\mathbf{P}}$, we have performed the measurements of $R_{2\omega}$ in varying orientations of the magnetic field rotated in the ab , bc , and ac planes. The results are shown in Fig. 2, where $R_{2\omega}$ is normalized by $R_0 B$ to factor out the change in the reciprocal response [19]. In both the ab - and bc -plane rotations, $R_{2\omega}/(R_0 B)$ at very low field, 0.03 T, shows a $\cos \theta$ dependence (θ is measured from the b axis), while $R_{2\omega}/(R_0 B)$ remains essentially zero in the ac -plane rotation. Since \mathbf{I} is along the a axis, this result indicates that $\hat{\mathbf{P}}$ is along the c axis. Detailed magnetic-field-orientation dependencies of ρ_{xx} [19] suggest that inversion symmetry is broken and, in particular, ab and ac are not mirror planes while bc is likely still a mirror plane. This suggests the lowering of the crystal symmetry from the space group $Cmcm$ to Cm . To corroborate this conclusion, we performed comprehensive single-crystal x-ray diffraction (XRD) studies, which actually detected broken inversion symmetry at room temperature [19]. The main distortion to break the inversion symmetry was found to be staggered displacements of Te3 atoms along the c axis [19]. No further symmetry breaking was detected between 30 to 300 K.

As shown in the inset of Fig. 2(a), the value of $|\gamma'| = 2A_{\perp} |R_{2\omega}/(R_0 B I_0)|$ for $B \parallel b$ axis [19] is strongly enhanced at low fields and reaches $4 \times 10^{-7} \text{ m}^2 \text{ T}^{-1} \text{ A}^{-1}$, which is gigantic [1]. In the following, we focus on the behavior at low fields. The behavior of $R_{2\omega}$ in high magnetic fields (in the ultraquantum limit) is much more complicated and requires a separate study [19].

The MCA is triggered by the combined effect of crystalline symmetry breaking and an external magnetic

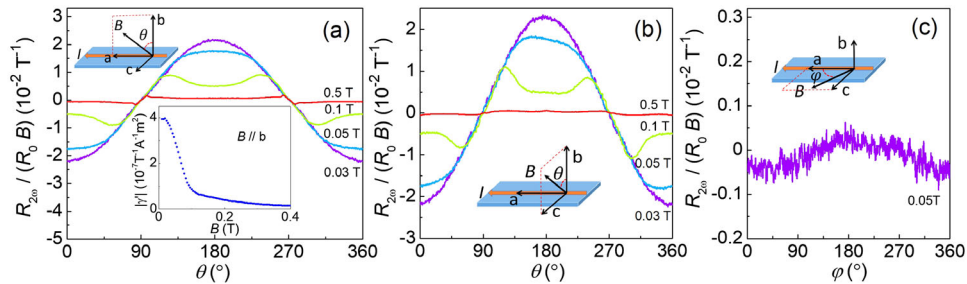


FIG. 2. Symmetry of the second-harmonic signal. (a)–(c) Magnetic-field-orientation dependencies of $R_{2\omega}/(R_0 B)$ in sample A measured at 3 K in 0.03, 0.05, 0.1, and 0.5 T [except for (c) which is only for 0.05 T] as the magnetic field was rotated in the ab , bc , and ac planes. The rotation plane and the definition of the angle (θ or φ) are shown in each panel. The lower inset of (a) shows the B dependence of $|\gamma'| [\equiv 2A_{\perp} |R_{2\omega}/(R_0 B I_0)|]$.

field. To explore whether the gigantic effect can be explained within existing theories [4] which focus on effects arising from the field-induced deformation of the Fermi surface, it is essential to identify both experimentally and theoretically the relevant band structure. The topological semimetal state of ZrTe_5 is usually considered to be a 3D Dirac semimetal in zero magnetic field [9] and it was claimed, based on the observation of negative longitudinal magnetoresistance [10] and anomalous Hall effect [12], that a Weyl semimetal state is realised in magnetic field. To derive an effective low-energy Hamiltonian, we start from the Dirac semimetal obtained in Ref. [9] based on symmetry arguments and comparison with band-structure calculations [7] assuming a high-symmetry $Cmcm$ space group. It is formulated using the basis states ($|\Psi_+^\uparrow\rangle, |\Psi_+^\downarrow\rangle, |\Psi_-^\uparrow\rangle, |\Psi_-^\downarrow\rangle$), where the \pm index describes linear combinations of Te p_y orbitals of even and odd parity [9]. Taking all experimentally observed symmetry breaking into account, we arrive at the following minimal model to describe ZrTe_5 [19]

$$H = m\mathbb{1} \otimes \tau_z + \hbar(v_a k_a \sigma_z \otimes \tau_x + v_b k_b \sigma_x \otimes \tau_x + v_c k_c \mathbb{1} \otimes \tau_y) + \Delta \mathbb{1} \otimes \tau_x + \xi \sigma_x \otimes \tau_y - \mu \mathbb{1}. \quad (1)$$

Here the space of the four lowest bands is spanned by 4×4 matrices of the form $\sigma_\alpha \otimes \tau_\beta$ where the Pauli matrices σ_α and τ_β act on the spin and parity space, respectively. The mass of the Dirac bands, m , is approximately tuned to zero in our samples of ZrTe_5 such that we consider $m = 0$ throughout. Importantly, the constant terms Δ and ξ describe the effect of ab - and ac -mirror symmetry breaking (respectively) as indicated by our experimental probes. A finite Δ or ξ splits the Dirac point into two massive bands and a nodal line [19]. The nodal line lies in a plane rotated about the a axis from the ab plane by the angle θ_{tilt} , defined via $\cos \theta_{\text{tilt}} = [\Delta / (\sqrt{\Delta^2 + v_b^2 \xi^2 / v_c^2})] \approx 1 - [(v_b^2 \xi^2) / 2\Delta^2 v_c^2]$. However, in ZrTe_5 the Fermi velocities satisfy $v_c \gg v_b$ and so the angle θ_{tilt} is likely very small (indeed we determine experimentally that $\theta_{\text{tilt}} \lesssim 1^\circ$, see below). Upon doping the system slightly, one obtains a Fermi surface with a torus shape wrapping around the nodal line, see Fig. S15 in the Supplemental Material [19].

We now consider how the torus Fermi surface can explain the presence of MCA. In the experimentally relevant case $\theta_{\text{tilt}} \approx 0$, the spin is locked to the momentum such that its orientation is $-(\hat{\mathbf{a}} \sin \phi + \hat{\mathbf{b}} \cos \phi)$, i.e., always parallel to the nodal line plane (ϕ is the polar angle in the ab plane), and the chirality of this texture is controlled by the sign of Δ . A magnetic field in the b direction (z axis) provides additional Zeeman energy that leads to a distortion of the Fermi surface necessary for obtaining nonreciprocal transport where the vector $\hat{\mathbf{P}}$ is set by the spin texture such that it is parallel to the normal of the plane containing the nodal line (i.e., parallel to the c direction). We have adapted the theory of Ref. [4] to this situation and also explored a novel

mechanism for nonreciprocal transport due to the anisotropic scattering resulting from the matrix-element effects [19]. In both cases, we obtain a nonreciprocal response of the form

$$|\gamma'| \approx \eta \frac{3g_b \mu_B}{8\pi e v_a n \Delta}, \quad (2)$$

where $g_b \approx 20$ is the g factor for a field in the b direction [9,16,36], e the electron charge, and $\Delta \gg \mu$ such that there is only a single Fermi surface. We find $\eta = 1$ for the mechanism of Ref. [4] and $\eta = 3$ for the anisotropic scattering. For both mechanisms, γ' will be strongly enhanced in the limit of small symmetry breaking Δ and small carrier doping with density n . In other words, a substantial MCA is expected only when both Δ and μ are very small.

Because the torus shape of the Fermi surface predicted from the broken mirror symmetries is crucial for the presence of MCA, we have performed quantum oscillation experiments, which would allow us to estimate the parameters for Eq. (2). For this purpose, we have grown a new batch of single crystals that are cleaner than sample A to observe quantum oscillations. One of such crystals (sample B) not only reproduced the gigantic $R_{2\omega}$ [Fig. 3(a)] but also presented clear Shubnikov-de Haas (SdH) oscillations [Figs. 3(a) and 3(b)]; the oscillations were observed only at low fields, because the Fermi surface is extremely small and the system enters the ultraquantum limit already at ~ 1 T for $B \parallel b$ axis. The evolution of the SdH-oscillation data when the direction of the B field was rotated within the bc plane is shown in Fig. 3(d), with their Fourier transforms presented in Figs. 3(e) and 3(f) (see Ref. [19] for details). Since the putative torus Fermi surface is expected to lie approximately in the ab plane, one would expect a switching of the extremal orbits [from δ and γ to α and β illustrated in Fig. 3(c) inset] above a critical angle when the B -field direction approaches the c axis [37]. In fact, multiple frequencies were observed for most of the field orientations and their angle dependencies show a break between 85° and 87° [Fig. 3(c)]; both observations are at odds with an elliptical Fermi surface but consistent with a torus Fermi surface [37]. From our fits we obtain a tiny electron density $n \approx 2.3 \times 10^{16} \text{ cm}^{-3}$ corresponding to the chemical potential $\mu = 4.9 \text{ meV}$, a small value for $\Delta \approx 19.1 \text{ meV}$, and determine $\theta_{\text{tilt}} \lesssim 1^\circ$ [19]. The extremely small μ implies that the Fermi surface is thermally smeared already at ~ 50 K, explaining why MCA diminishes with increasing T in Fig. 1(d).

Using the parameters that explain the dispersion in the SdH-oscillation data [19], we find Eq. (2) predicts $|\gamma'| \sim 1 \times 10^{-11} \text{ m}^2 \text{ A}^{-1} \text{ T}^{-1}$. This is a relatively large value compared to other materials but four orders of magnitude smaller than our measured value. We conclude that the deformation of the Fermi surface by the Zeeman effect is not sufficient to explain the gigantic MCA. We have also checked [19] that orbital effects of the magnetic field and

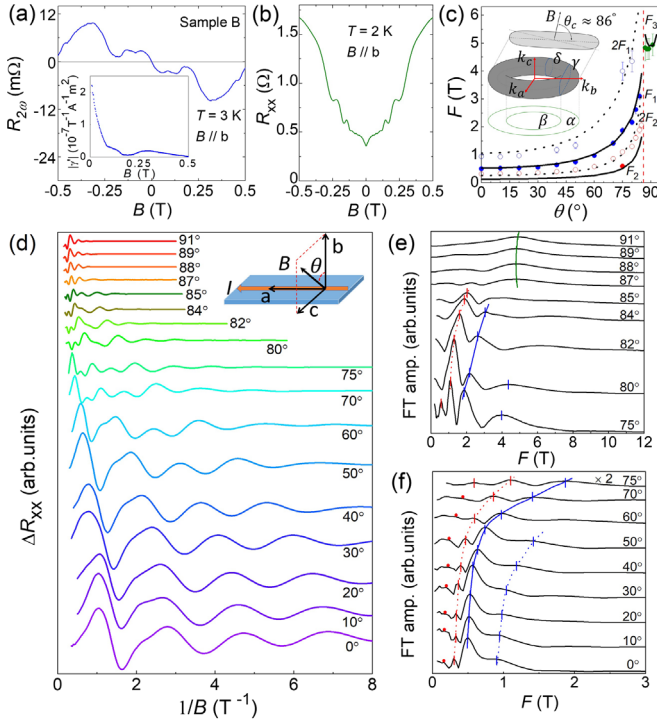


FIG. 3. Shubnikov–de Haas (SdH) oscillations. (a) Magnetic-field dependence of $R_{2\omega}$ for sample B measured in $B \parallel b$ at 3 K; inset shows the B dependence of the calculated $|\gamma'|$. (b) Resistance component R_{xx} measured across a transverse electrode pair [19]. (c) Experimentally observed SdH frequencies (symbols) and the theoretical fits based on the torus Fermi surface (lines); inset shows the schematic diagram of a torus Fermi surface and its extremal orbits α , β , δ , and γ . As discussed in detail in Ref. [19], the frequencies F_1 , F_2 , and F_3 correspond to γ , δ , and β orbits, respectively, and $2F_1$ ($2F_2$) is the second harmonic of F_1 (F_2); error bars are shown only when they are larger than the symbol size. (d) SdH oscillations in magnetic fields rotated in the bc plane, measured in R_{xx} after subtracting a smooth background. (e), (f) Results of Fourier transforms of the SdH oscillations; ticks mark obvious peaks, and red dots mark the expected position of F_2 based on its 2nd harmonic, $2F_2$.

further perturbations of the minimal model Eq. (1) cannot naturally explain such a large effect.

A likely mechanism giving rise to the giant enhancement of nonlinear transport in ZrTe_5 are large-scale fluctuations in the electronic density as they may arise due to the unavoidable presence of charged impurities [38,39]. In regions of low density, local electric fields and therefore nonlinear effects can be strongly enhanced [19]. Two experimental observations strongly support such a scenario in ZrTe_5 . First, inhomogeneities triggered by charged impurities may naturally form in ZrTe_5 due to the extremely small carrier density of only 5×10^{-6} electrons per formula unit ($2.3 \times 10^{16} \text{ cm}^{-3}$), which also suppresses screening. Second, more directly, a comparison of our quantum oscillation data to resistivity reveals that the measured resistivity is much higher than that expected for

a homogeneous material; namely, we found that the transport scattering rate extracted from the resistivity is almost an order of magnitude larger than the scattering rates obtained from the decay of SdH oscillations [19]. This is naturally understood by assuming that transport is forced to occur through regions with high resistivity, while quantum oscillations arise from areas with fewer scattering events and lower resistivity. The anisotropic Fermi velocities characteristic for ZrTe_5 and the resulting quasi-one-dimensional transport are also of relevance for this effect as it suppresses electron flow around obstacles.

The reproducibility of this striking phenomenon is confirmed in 10 more samples showing the resistivity maximum close to 0 K [19], which all presented $|\gamma'|$ of similar order. Nevertheless, its exact value varied among samples and we found no clear correlation between the residual resistivity ρ_0 and $|\gamma'|$; such a strong sample dependence is consistent with the puddle scenario. Note that we did not intentionally introduce impurities and their distribution is random. The sign of γ' was also sample dependent, suggesting that the sign of the $\hat{\mathbf{P}}$ vector is randomly fixed, possibly by an anisotropic strain created upon cooling. In samples having the resistivity-peak temperature T_p of 15–50 K, a finite $|\gamma'|$ which decreases with T was observed, but $|\gamma'|$ was no longer discernible in samples with $T_p \approx 130$ K [19]. The suppression of $|\gamma'|$ in higher T_p samples most likely originates from an increased carrier density of those samples which also suppresses large density fluctuations.

In conclusion, close to the topological phase transition, ZrTe_5 is a topological semimetal with a torus-shaped Fermi surface. As a result of the proximity to the topological phase transition, this Fermi surface possesses a spin texture that specifies the $\hat{\mathbf{P}}$ vector responsible for a large MCA, which is further enhanced by large-scale electron density fluctuations in ZrTe_5 . This intriguing finding points to rich physics in nonreciprocal transport taking place in topological materials with extremely low carrier density.

This project has received funding from the European Research Council (ERC) under the European Union’s Horizon 2020 research and innovation programme (Grant Agreement No. 741121) and was also funded by the Deutsche Forschungsgemeinschaft (DFG, German Research Foundation) under CRC 1238—277146847 (Subprojects A02, A04 and C02) as well as under Germany’s Excellence Strategy—Cluster of Excellence Matter and Light for Quantum Computing (ML4Q) EXC 2004/1—390534769.

*ando@ph2.uni-koeln.de

- [1] Y. Tokura and N. Nagaosa, *Nat. Commun.* **9**, 3740 (2018).
- [2] G. L. J. A. Rikken, J. Folling, and P. Wyder, *Phys. Rev. Lett.* **87**, 236602 (2001).

- [3] G. L. J. A. Rikken and P. Wyder, *Phys. Rev. Lett.* **94**, 016601 (2005).
- [4] T. Ideue, K. Hamamoto, S. Koshikawa, M. Ezawa, S. Shimizu, Y. Kaneko, Y. Tokura, N. Nagaosa, and Y. Iwasa, *Nat. Phys.* **13**, 578 (2017).
- [5] G. L. J. A. Rikken and N. Avarvari, *Phys. Rev. B* **99**, 245153 (2019).
- [6] T. Morimoto and N. Nagaosa, *Phys. Rev. Lett.* **117**, 146603 (2016).
- [7] H. Weng, X. Dai, and Z. Fang, *Phys. Rev. X* **4**, 011002 (2014).
- [8] B. Xu, L. X. Zhao, P. Marsik, E. Sheveleva, F. Lyzwa, Y. M. Dai, G. F. Chen, X. G. Qiu, and C. Bernhard, *Phys. Rev. Lett.* **121**, 187401 (2018).
- [9] R. Y. Chen, Z. G. Chen, X. Y. Song, J. A. Schneeloch, G. D. Gu, F. Wang, and N. L. Wang, *Phys. Rev. Lett.* **115**, 176404 (2015).
- [10] Q. Li, D. E. Kharzeev, C. Zhang, Y. Huang, I. Pletikosic, A. V. Fedorov, R. D. Zhong, J. A. Schneeloch, G. D. Gu, and T. Valla, *Nat. Phys.* **12**, 550 (2016).
- [11] Y. Zhang *et al.*, *Nat. Commun.* **8**, 15512 (2017).
- [12] T. Liang, J. Lin, Q. Gibson, S. Kushwaha, M. Liu, W. Wang, H. Xiong, J. A. Sobota, M. Hashimoto, P. S. Kirchmann, Z.-X. Shen, R. J. Cava, and N. P. Ong, *Nat. Phys.* **14**, 451 (2018).
- [13] H. Wang, H. Liu, Y. Li, Y. Liu, J. Wang, J. Liu, J.-Y. Dai, Y. Wang, L. Li, J. Yan, D. Mandrus, X. C. Xie, and J. Wang, *Sci. Adv.* **4**, eaau5096 (2018).
- [14] P. Shahi, D. J. Singh, J. P. Sun, L. X. Zhao, G. F. Chen, Y. Y. Lv, J. Li, J. Q. Yan, D. G. Mandrus, and J. G. Cheng, *Phys. Rev. X* **8**, 021055 (2018).
- [15] F. Tang, Y. Ren, P. Wang, R. Zhong, J. Schneeloch, S. A. Yang, K. Yang, P. A. Lee, G. Gu, Z. Qiao, and L. Zhang, *Nature (London)* **569**, 537 (2019).
- [16] Z. Sun, Z. Cao, J. Cui, C. Zhu, D. Ma, H. Wang, W. Zhuo, Z. Cheng, Z. Wang, X. Wan, and X. Chen, *npj Quantum Mater.* **5**, 36 (2020).
- [17] B. Fu, H.-W. Wang, and S.-Q. Shen, *Phys. Rev. Lett.* **125**, 256601 (2020).
- [18] C. Wang, *Phys. Rev. Lett.* **126**, 126601 (2021).
- [19] See Supplemental Material at <http://link.aps.org/supplemental/10.1103/PhysRevLett.128.176602> for additional data and discussion, which includes Refs. [20–31].
- [20] N. P. Armitage, E. J. Mele, and A. Vishwanath, *Rev. Mod. Phys.* **90**, 015001 (2018).
- [21] Y. Ando, *J. Phys. Soc. Jpn.* **82**, 102001 (2013).
- [22] D. Shoenberg, *Magnetic Oscillations in Metals* (Cambridge University Press, Cambridge, England, 2009).
- [23] H. Yang, R. Moessner, and L.-K. Lim, *Phys. Rev. B* **97**, 165118 (2018).
- [24] A. Alexandradinata and L. Glazman, *Phys. Rev. B* **97**, 144422 (2018).
- [25] S. Furuseth, L. Brattas, and A. Kjekshus, *Acta Chem. Scand.* **27**, 2367 (1973).
- [26] E. F. Skelton, T. J. Wieting, S. A. Wolf, W. W. Fuller, D. U. Gubser, T. L. Francavilla, and F. Levy, *Solid State Commun.* **42**, 1 (1982).
- [27] T. Sambongi, Pentachalcogenides of transition metals, in *Crystal Chemistry and Properties of Materials with Quasi-One-Dimensional Structures: A Chemical and Physical Synthetic Approach*, edited by J. Rouxel (Springer Netherlands, Dordrecht, 1986), pp. 281–313.
- [28] H. Fjellvag and A. Kjekshus, *Solid State Commun.* **60**, 91 (1986).
- [29] J. Smit, *Physica (Utrecht)* **24**, 39 (1958).
- [30] O. Breunig, Z. Wang, A. A. Taskin, J. Lux, A. Rosch, and Y. Ando, *Nat. Commun.* **8**, 15545 (2017).
- [31] Y.-Y. Lv, F. Zhang, B.-B. Zhang, B. Pang, S.-H. Yao, Y. B. Chen, L. Ye, J. Zhou, S.-T. Zhang, and Y.-F. Chen, *J. Cryst. Growth* **457**, 250 (2017).
- [32] H. A. Hafez, S. Kovalev, J.-C. Deinert, Z. Mics, B. Green, N. Awari, M. Chen, S. Germanskiy, U. Lehnert, J. Teichert, Z. Wang, K.-J. Tielrooij, Z. Liu, Z. Chen, A. Narita, K. Müllen, M. Bonn, M. Gensch, and D. Turchinovich, *Nature (London)* **561**, 507 (2018).
- [33] Z. Sun, Y. Yi, T. Song, G. Clark, B. Huang, Y. Shan, S. Wu, D. Huang, C. Gao, Z. Chen, M. McGuire, T. Cao, D. Xiao, W.-T. Liu, W. Yao, X. Xu, and S. Wu, *Nature (London)* **572**, 497 (2019).
- [34] S. Kovalev, R. M. A. Dantas, S. Germanskiy, J.-C. Deinert, B. Green, I. Ilyakov, N. Awari, M. Chen, M. Bawatna, J. Ling, F. Xiu, P. H. M. van Loosdrecht, P. Surówka, T. Oka, and Z. Wang, *Nat. Commun.* **11**, 2451 (2020).
- [35] B. Cheng, N. Kanda, T. N. Ikeda, T. Matsuda, P. Xia, T. Schumann, S. Stemmer, J. Itatani, N. P. Armitage, and R. Matsunaga, *Phys. Rev. Lett.* **124**, 117402 (2020).
- [36] Y. Liu, X. Yuan, C. Zhang, Z. Jin, A. Narayan, C. Luo, Z. Chen, L. Yang, J. Zou, X. Wu, S. Sanvito, Z. Xia, L. Li, Z. Wang, and F. Xiu, *Nat. Commun.* **7**, 12516 (2016).
- [37] Y. H. Kwan, P. Reiss, Y. Han, M. Bristow, D. Prabhakaran, D. Graf, A. McCollam, S. A. Parameswaran, and A. I. Coldea, *Phys. Rev. Research* **2**, 012055(R) (2020).
- [38] B. Skinner, T. Chen, and B. I. Shklovskii, *Phys. Rev. Lett.* **109**, 176801 (2012).
- [39] N. Borgwardt, J. Lux, I. Vergara, Z. Wang, A. A. Taskin, K. Segawa, P. H. M. van Loosdrecht, Y. Ando, A. Rosch, and M. Grüninger, *Phys. Rev. B* **93**, 245149 (2016).